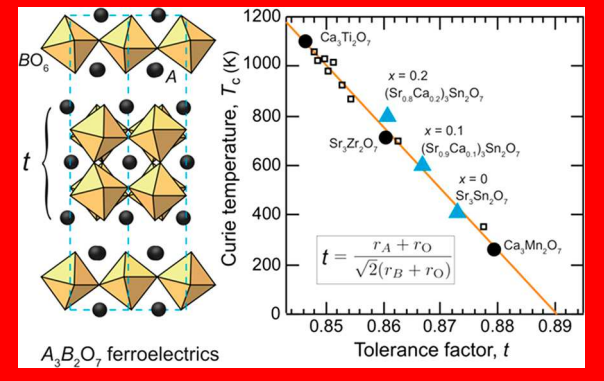


Hybrid Improper Ferroelectricity in (Sr,Ca)₃Sn₂O₇ and Beyond: Universal Relationship between Ferroelectric Transition Temperature and Tolerance Factor in n = 2 Ruddlesden-Popper **Phases**

Suguru Yoshida,[†] Hirofumi Akamatsu,^{‡,O} Ryosuke Tsuji,[†] Olivier Hernandez,^{||} Haricharan Padmanabhan,[‡] Arnab Sen Gupta,[‡] Alexandra S. Gibbs,[⊥] Ko Mibu,[#] Shunsuke Murai,[†] James M. Rondinelli,[∇] Venkatraman Gopalan,^{‡,§} Katsuhisa Tanaka,[†] and Koji Fujita*,[†]

Supporting Information

Hybrid improper ferroelectricity, which utilizes nonpolar but ubiquitous rotational/tilting distortions to create polarization, offers an attractive route to the discovery of new ferroelectric and multiferroic materials because its activity derives from geometric rather than electronic origins. Design approaches blending group theory and first principles can be utilized to explore the crystal symmetries of ferroelectric ground states, but in general, they do not make accurate predictions for some important parameters of ferroelectrics, such as Curie temperature $(T_{\rm C})$. Here, we establish a predictive and quantitative relationship between T_C and the Goldschmidt tolerance factor, t, by employing n = 2 Ruddlesden-Popper (RP) A₃B₂O₇ as a prototypical example of hybrid improper ferroelectrics. The focus is placed on an RP system, $(Sr_{1-x}Ca_x)_3Sn_2O_7$ (x = 0, 0.1, and 0.2), which allows for the investigation of the purely



geometric (ionic size) effect on ferroelectric transitions, due to the absence of the second-order Jahn–Teller active (d⁰ and 6s²) cations that often lead to ferroelectric distortions through electronic mechanisms. We observe a ferroelectric-to-paraelectric transition with $T_C = 410$ K for $Sr_3Sn_2O_7$. We also find that the T_C increases linearly up to 800 K upon increasing the Ca^{2-} content, i.e., upon decreasing the value of t. Remarkably, this linear relationship is applicable to the suite of all known $A_3B_2O_7$ hybrid improper ferroelectrics, indicating that the T_C correlates with the simple crystal chemistry descriptor, t_i based on the ionic size mismatch. This study provides a predictive guideline for estimating the T_C of a given material, which would complement the convergent group-theoretical and first-principles design approach.

1. INTRODUCTION

Since the discovery of ceramic BaTiO3, ferroelectricity has been an attractive topic in material science and engineering due to theoretical interest and its industrial applications. This field of research has long been centered on ABO3 perovskites, the family members of the first ferroelectric oxide. The most common mechanism for creating perovskite ferroelectrics lies in collective ionic displacements of electronic origin, typically driven by off-centering of the A- and/or B-site cations via the

second-order Jahn-Teller (SOJT) effect.²⁻⁴ However, the SOJT effect is usually favorable for *n*d⁰ transition-metal cations (Ti⁴⁺, Nb⁵⁺, Ta⁵⁺) or 6s² post-transition metal cations (Pb²⁺, Bi³⁺),^{5,6} and some compounds never become ferroelectric, even in the presence of these SOJT-active cations. 7-10 The strict chemical requirement is problematic for the general-

Received: July 27, 2018 Published: October 23, 2018



[†]Department of Material Chemistry, Graduate School of Engineering, Kyoto University, Katsura Nishikyo-ku, Kyoto 615-8510, Japan

^{*}Materials Research Institute and Department of Materials Science and Engineering and [§]Department of Physics, Pennsylvania State University, University Park, Pennsylvania 16802, United States

Univ Rennes, CNRS, ISCR (Institut des Sciences Chimiques de Rennes) - UMR 6226, F-35000 Rennes, France

[⊥]ISIS Pulsed Neutron and Muon Source, STFC Rutherford Appleton Laboratory, Harwell Campus, Didcot OX11 0QX, U.K.

Department of Physical Science and Engineering, Nagoya Institute of Technology, Gokiso-cho, Showa-ku, Nagoya, 466-8555, Japan $^{
abla}$ Department of Materials Science and Engineering, Northwestern University, 2220 Campus Drive, Evanston, Illinois 60208-3108, United States

Journal of the American Chemical Society

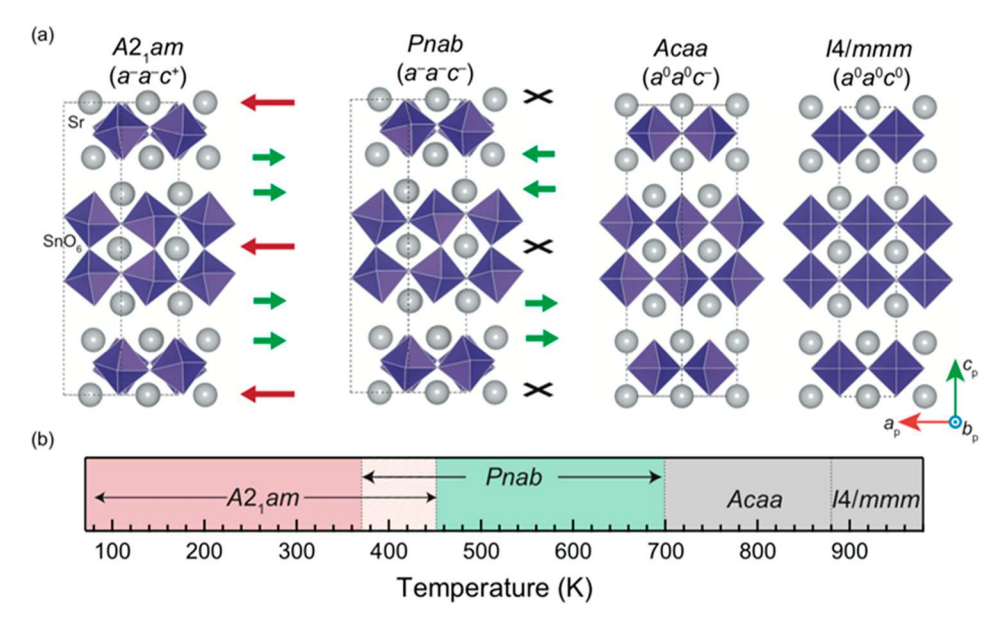


Figure 1. (a) The crystal structures of four phases observed experimentally for $Sr_3Sn_2O_7$ are illustrated, specified by the space group symmetry and Glazer tilt notation. Gray spheres and blue octahedra denote the Sr cations and SnO_6 octahedra, respectively. Black dotted lines indicate the unit cells. For $A2_1am$ and Pnab phases, local electric dipoles that arise from Sr cation displacements are shown by red and green arrows. Black cross marks indicate that there are no Sr displacements and thus no layer polarization. (b) The phase diagram of $Sr_3Sn_2O_7$ established in the present study.

ization of the design guidelines, making it challenging to straightforwardly synthesize ABO₃ ferroelectrics.

Recent theoretical work has developed a new mechanism for achieving a ferroelectric state, whereby two nonpolar structural distortions, commonly rotations or tilts of BO6 octahedra, cooperatively give rise to a net polar symmetry and induce a macroscopic polarization as a byproduct. 11-13 This novel mechanism, called hybrid improper ferroelectricity, 11,14 is active in layered perovskite oxides like Ruddlesden-Popper (RP)^{15,16} and Dion-Jacobson phases¹⁷ and has opened a new avenue for the rational design of ferroelectric materials. 18-20 This form of ferroelectricity, of geometric origin, should be prevalent in perovskite-related compounds, because the octahedral rotations/tilts are ubiquitous structural distortions²¹ (which are predominantly driven by the size mismatch of the constituent ions). Indeed, a number of layered perovskites have been proposed as potential hybrid improper ferroelectrics through the integrated approach of symmetry arguments and first-principles calculations, 22-30 some of which have been experimentally confirmed to exhibit switchable polarization^{31–38} or at least crystallize in polar structures.^{39–46} One can now utilize group theory to elucidate symmetry breaking caused by given distortions and identify whether their combinations result in a polar symmetry and then the ferroelectricity. For real technological applications, on the other hand, it is important to evaluate key parameters of ferroelectrics, including polarization, coercive field, and Curie temperature (T_C) . But, generally, it is not straightforward to calculate these parameters, in particular $T_{\rm C}$, with high precision through a combination of group-theoretical analysis and firstprinciples calculations.47

The Goldschmidt tolerance factor, t, is a simple chemistry descriptor for perovskite stability and is calculated by the following equation: $t = (r_A + r_O)/\sqrt{2(r_B + r_O)}$, where r_A , r_B , and r_O represent the ionic radii of A-site, B-site, and O^{2-} , respectively. In this paper, we study n = 2 RP $A_3B_2O_7$ (Figure 1a), a prototypical example of hybrid improper ferroelectrics,

and establish a predictive and quantitative relationship between $T_{\rm C}$ and t. In order to examine the pure effect of varying ionic size mismatch on T_C , we focus on $(Sr_{1-x}Ca_x)_3Sn_2O_7$ (x = 0, 0.1, and 0.2), RP compounds in the absence of SOJT-active cations. Sr₃Sn₂O₇ was recently reported as the first ferroelectric Sn insulator with switchable electric polarization;³⁶ however, its ferroelectric-to-paraelectric transition was not detected up to 1035 K. The relation between the ferroelectricity and the octahedral rotation/tilt has also not been clarified. Here, we successfully reveal a first-order ferroelectric-to-paraelectric transition from $A2_1am$ to Pnab symmetry in $Sr_3Sn_2O_7$ ($T_C =$ 410 K, Figure 1b) using powder neutron diffraction (ND) and synchrotron X-ray diffraction (SXRD), as well as optical second-harmonic generation (SHG). The experimental studies, complemented by first-principles density functional theory (DFT) calculations, allow us to identify the role played by the two nonpolar structural distortions—oxygen octahedral rotations (OOR, rotational modes about c axis) and oxygen octahedral tilts (OOT, rotational modes about the a and/or b axis)—in stabilizing the ferroelectric A21am and paraelectric Pnab structures. Our results demonstrate that the stable ferroelectric A2₁am phase appears through a trilinear coupling of OOR and OOT to the polar lattice mode (i.e., hybrid improper ferroelectric mechanism) and that the metastable Pnab polymorph, which competes with the ground-state A2₁am phase, emerges from a trilinear coupling of OOR and OOT interacting with an antipolar lattice mode (i.e., hybrid improper "antiferroelectric" mechanism). ^{37,50,51} Further, we observe that the T_C increases linearly with the substitution of Ca²⁺ for Sr²⁺. Remarkably, when we consider the 15 compounds including n = 2 RP ferroelectrics reported here and those reported previously elsewhere [Ca₃Ti₂O₇, ³² $Ca_3Mn_2O_7$, 40 $Sr_3Zr_2O_7$, 37 $(Ca,Sr)_3Ti_2O_7$, 3 $Ca_3Mn_2O_7$, $Ga_3(Ti,Mn)_2O_7$, $Ga_3(Ti,Mn)_2O_7$, a simple linear relationship is found between $T_{\rm C}$ and t, despite the diversity of chemical composition. It is surprising that the T_C strongly correlates with the simple chemistry descriptor, t, based on ionic size

mismatch. Our findings show the controllability of T_C in hybrid improper ferroelectrics and provide a rule of thumb for predicting the T_C of as yet unsynthesized materials that would complement the group-theoretical design strategy.

2. METHODS

Experimental Procedures. Polycrystalline samples of $(Sr_{1-x}Ca_x)_3Sn_2O_7$ (x = 0, 0.1, and 0.2) were synthesized by the solid-state reaction method. Reagent-grade SrCO₃ (99.9%), CaCO₃ (99.9%), and SnO₂ (99.9%) were mixed so as to obtain a stoichiometric composition, ground in an agate mortar, and pressed into a pellet. The pellet was calcinated at 1000 °C for 6 h and sintered at 1300 °C for 48 h. The resultant pellet was ground, thoroughly mixed, pelletized again, and sintered at 1500 °C for 6 h. The pellets were slowly cooled to room temperature.

High-resolution time-of-flight ND was performed using the HRPD diffractometer at the ISIS facility (Harwell Campus, UK); data at 300 K were collected for $(Sr_{1-x}Ca_x)_3Sn_2O_7$ (x = 0, 0.1, and 0.2), and data at higher temperatures (315–950 K) were recorded for $Sr_3Sn_2O_7$ ($\alpha =$ 0). Approximately 5 g of the finely ground powder sample was housed in a vanadium can with an inner diameter of 11 mm. Using three detection banks (backscattering bank, 90° bank, and low-angle bank), we obtained diffraction patterns over a time-of-flight range of 30-130 ms corresponding to a d-range of 0.65-9.0 Å. For 300 and 500 K, the diffraction patterns over a time-of-flight range of 100-200 ms were also recorded to observe the Bragg reflections at longer d-spacing. SXRD was carried out for $(Sr_{1-x}Ca_x)_3Sn_2O_7$ (x = 0, 0.1, and 0.2) in the temperature range of 300 to 900 K using the large Debye-Scherrer camera with MYTHEN solid-state detectors installed at SPring-8 BL02B2, Japan. The incident X-ray was monochromated at λ = 0.798 833 or 0.800 484 Å. The powder sample was housed in a Lindeman capillary tube with an inner diameter of 0.1 mm and rotated continuously during measurement to diminish the effect of preferred orientation. Above 800 K, we also utilized an SiO2 capillary tube with an inner diameter of 0.2 mm. The ND and SXRD data collected at the same temperatures were fitted simultaneously by the Rietveld 52 method with the FullProf suite; 53 otherwise, they were fitted separately.

Optical SHG was measured for $Sr_3Sn_2O_7$ (x = 0) in reflection geometry using a regeneratively amplified mode-locked Ti:sapphire laser (800 nm wavelength, 80 fs pulse duration, 1 kHz repetition rate). Temperature-dependent data were recorded in a heating and cooling cycle between 300 and 460 K using a home-built heater. Differential scanning calorimetry (DSC) was also recorded for the x = 0 sample from room temperature to 700 K by using a Rigaku Thermo Plus DSC 8270 at a heating rate of 10 K/min.

¹¹⁹Sn Mössbauer spectroscopy was performed at room temperature for $(Sr_{1-x}Ca_x)_3Sn_2O_7$ (x = 0, 0.1, and 0.2) in a transmission geometry using a $\text{Ca}^{119\text{m}}\text{SnO}_3$ γ -ray source. The source velocity and isomer shift were calibrated by α -Fe and CaSnO₃, respectively. The spectra were analyzed by least-squares fitting using Lorentzian functions.

First-Principles Calculations. We carried out DFT calculations for $Sr_3Sn_2O_7$ by using the projector augmented-wave (PAW) method 54,55 and PBEsol functional $^{56-58}$ as implemented in the VASP code. $^{59-62}$ We employed PAW data sets with radial cutoffs of 2.1, 1.6, and 0.8 Å for Sr, Sn, and O, respectively. A plane wave cutoff energy of 550 eV was utilized for structural optimization. We used a cutoff energy of 400 eV to obtain force constants for phonon calculations. The following states were regarded as valence states: Sr 4s, 4p, and 5s; Sn 4d, 5s, and 5p; O 2s and 2p. Lattice constants and fractional coordinates were optimized until the residual stress and forces converged down to 0.01 GPa and 1 meV/ Å, respectively.

Phonon frequencies and eigenvectors were calculated utilizing a frozen-phonon method as implemented in the PHONOPY code. The phonon dispersion curves were drawn for a standard primitive cell^{64,65} along a q-space path based on crystallography.⁶⁶ Our systematic stable structure exploration was conducted in a previously reported way. $^{37,67-70}$ Frequencies of the Brillouin zone-center phonon modes were calculated for a $\sqrt{2} \times \sqrt{2} \times 1$ supercell of the tetragonal conventional cell (space group I4/mmm) of aristotype phase with a 4 \times 4 \times 1 k-point mesh. We note that zone-boundary phonon modes at the X and M points for an I4/mmm primitive cell are included in the zone-center phonon modes for the supercell via band folding. When imaginary frequency phonon modes were found, we distorted the parent I4/mmm aristotype structure according to the eigenvectors of the unstable modes, optimized the structural parameters of the lowersymmetry structures, and calculated the phonon frequencies to see if there was any phonon instability. This process was iterated unless the obtained structure was found to be dynamically stable. The cell metric was fixed during the stable structure exploration.

For energy surface calculations, structural distortions were decomposed into symmetry-adapted modes of the parent I4/mmm phase using the AMPLIMODES⁷¹ tool available at the Bilbao Crystallographic Server. The mode amplitude is defined as the square root of the sum of squared displacement vectors. The distortion patterns were visualized by the VESTA code.

3. RESULTS

Room-Temperature Structure of Sr₃Sn₂O₇. Although the room-temperature structure of Sr₃Sn₂O₇ was believed to be orthorhombic with space group Amam, 73 rerecent work using laboratory X-ray diffraction and dark-field transmission electron microscopy reported that this compound crystallizes in orthorhombic space group A2₁am at 300 K.³⁶ We also revisit the crystal structure at 300 K by using highresolution ND, which allows a much more accurate determination of oxygen parameters than X-ray methods. Although the main reflections of the ND pattern at 300 K can be indexed with the tetragonal I4/mmm aristotype structure, additional $h+^{1}/_{2}k+^{1}/_{2}l$ superlattice reflections (e.g., $^{3}/_{2}^{3}/_{2}3$ reflection and $\frac{5}{2}\frac{1}{2}$ reflection in Figure 2a,b) are observed,

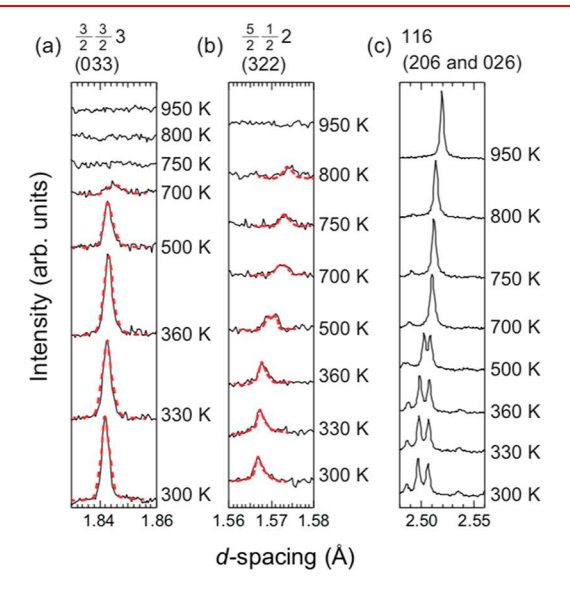
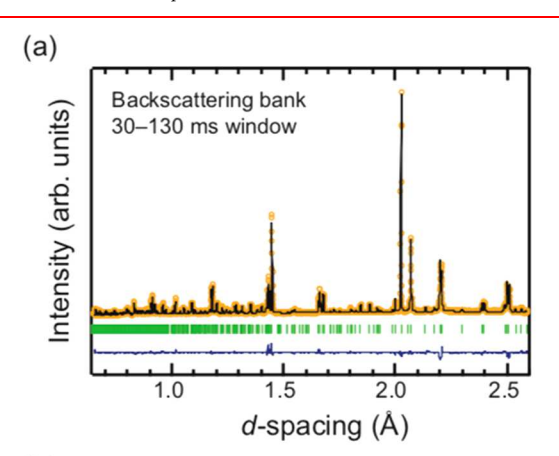


Figure 2. Temperature evolution of ND (a) $\frac{3}{2}\frac{3}{2}$ superlattice reflection, (b) $\frac{5}{2}/\frac{1}{2}$ superlattice reflection, and (c) basic 116 reflection observed for Sr₃Sn₂O₇. Miller indices with respect to the $\sqrt{2a_p} \times \sqrt{2a_p} \times c_p$ unit cell are given in parentheses.

together with the splitting of basic hhl reflections (e.g., basic 116 reflection in Figure 2c). The superlattice reflections and reflection splittings are also found in the SXRD pattern at 300 K. These features indicate the symmetry-lowering from tetragonal to orthorhombic with an enlarged unit cell metric, $\sqrt{2a_p} \times \sqrt{2a_p} \times c_p$, where a_p and c_p are the pseudotetragonal lattice parameters. The larger cell was also reported in the previous works.^{36,73} Note that no impurity phases were detected from either ND or SXRD data.

The observed reflection conditions in the orthorhombic setting are hkl: k + l = 2n; 0kl: k + l = 2n; h0l: h, l = 2n; hk0: k= 2n; h00: h = 2n; 0k0: k = 2n; and 00l: l = 2n (n = integer). Noncentrosymmetric and polar A21am and centrosymmetric and nonpolar Amam space groups have been derived from the reflection conditions and the compatibility with n = 2 RP structures. The structural model in A21am symmetry involves two distinct OOT and OOR, represented by $a^-a^-c^0$ and $a^0a^0c^+$, respectively, in Glazer notation, 74 whereas the Amam structure only involves $a^-a^-c^0$ -type OOT. These out-of-phase OOT and in-phase OOR modes transform as the irreducible representation (irrep) X_3^- , and X_2^+ of I4/mmm, respectively. The Rietveld refinement with a polar A21am structural model against the ND pattern results in an excellent overall fit ($R_{wp} = 13.4\%$, see Figure 3a), while the Amam model cannot reproduce some observed peak intensities, for example, hk0 ($h \neq 2n$, and k =2n) reflections ($R_{wp} = 16.3\%$, see Figure 3b). The SXRD



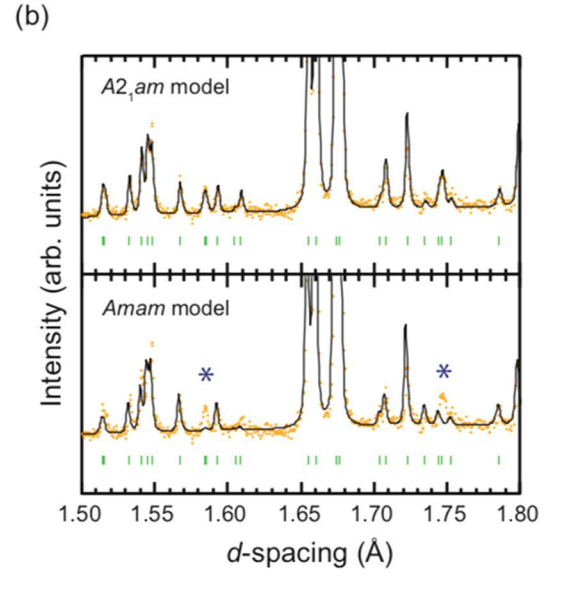


Figure 3. (a) Rietveld plot of ND data at 300 K for Sr₂Sn₂O₇ refined with a ferroelectric A21am structural model. (b) An enlarged view of Rietveld plots of 300 K ND data for Sr₃Sn₂O₇ refined with A2₁am and Amam structural models. Mismatches between the observed and calculated intensities are marked with asterisks. Orange circles and black and blue lines represent the observed, calculated, and difference profiles, respectively. The green ticks show the position of Bragg reflections.

pattern is also fitted better with the A2₁am model [Figure S1, Supporting Information (SI)]. On the basis of these results, we assign the crystal symmetry of Sr₃Sn₂O₇ at 300 K to the polar

This assignment is further verified by SHG measurement, which is a powerful technique to probe inversion symmetry breaking in piezoelectrics, pyroelectrics, and ferroelectrics. A significant SHG signal is clearly observed over the temperature range from 300 K to about 400 K (see next subsection), indicating the absence of the inversion symmetry, i.e. the polar crystal structure with A21am symmetry in this case. Our diffraction and optical experiments thus prove that Sr₃Sn₂O₇ crystallizes in polar A2₁am symmetry at 300 K, in agreement with the previous work by Wang et al.³⁶ and our systematic stable structure exploration (see section S4, SI).

We also checked the deviation in the stoichiometry. During combined Rietveld analysis against 300 K ND and SXRD data, the cation and anion site occupancies in the A21am model were refined, but the refined occupancies were consistently within 1 or 2% of the expected values. Hence, the site occupancies were fixed at unity for all the sites in the final refinement. The structural parameters of the A21am phase at 300 K obtained from joint refinements against the ND and SXRD data are listed in Table 1. We estimated the octahedral distortion in

Table 1. Structural Parameters of Sr₃Sn₂O₇ at 300 K Obtained from Joint Refinements with an A21am Model against ND and SXRD Data^a

atom	site	x	у	z	$U_{ m iso} { m or}_{ m eq} U_{ m eq} \ ({ m \AA}^2)$
O1	4 <i>a</i>	0.2505(19)	0.7996(10)	0	0.0110(12)
O2	8b	0.2597(13)	0.7091(6)	0.19631(10)	0.0059(7)
O3	8b	0.5280(15)	0.5295(8)	0.08689(12)	0.0038(8)
O4	8b	0.4842(18)	0.0143(10)	0.10565(13)	0.0142(8)
Sr1 ^c	4 <i>a</i>	0.2548(19)	0.2491(10)	0	0.0109(14)
Sr2 ^c	8b	0.7374(10)	0.7431(5)	0.18846(6)	0.0080(10)
Sn	8b	0.75 ^b	0.2492(6)	0.09854(6)	0.0018(2)

^aSpace group $A2_1am$ (No. 36), Z = 4. The occupancy parameter is fixed to unity for all atoms. ^bFixed to define an origin of the polar a axis. Refined anisotropically. Cell parameters: a = 5.70739(10) Å, b =5.73485(10) Å, and c = 20.66861(5) Å. ND: $R_{\rm wp} = 11.5\%$, $R_{\rm B} = 7.85\%$, and $\chi^2 = 4.89$. SXRD: $R_{\rm wp} = 12.7\%$, $R_{\rm B} = 3.80\%$, and $\chi^2 = 6.34$.

 $Sr_3Sn_2O_7$ using the octahedral distortion parameter, Δ = $^{1}/_{6}\sum_{i}[(d_{i}-\langle d\rangle)/\langle d\rangle]^{2}$, where d_{i} is the individual Sn–O bond length and $\langle d \rangle$ is the mean bond length in SnO₆ octahedra. We obtained $\Delta = 4.1 \times 10^{-5}$ for SnO₆ in Sr₃Sn₂O₇, which is smaller than that for TiO_6 ($\Delta = 1.6 \times 10^{-4}$) in $Ca_3Ti_2O_{7}^{32}$ where the SOJT effect of Ti⁴⁺(3d⁰) ions leads to off-centering distortion of TiO₆ octahedra. Note that Sn⁴⁺ (4d¹⁰) is not SOJT-active, in contrast to Sn²⁺ (which has a 5s² lone pair of

Further, we performed 119Sn Mössbauer spectroscopy at room temperature to evaluate the valence state and local structure of tin ions. The result for Sr₃Sn₂O₇ is shown in Figure 4. Stannous (Sn²⁺) and stannic (Sn⁴⁺) compounds are wellknown to differ widely in isomer shift on account of the difference in the oxidation state; the isomer shift values for Sn²⁺ ions (2.3 to 4.5 mm/s) are always higher than those for Sn⁴⁺ ions (-0.4 to 2.3 mm/s).⁷⁶ In the present case, a single broadened peak is observed with the isomer shift (approximately 0 mm/s) typical of Sn⁴⁺-containing compounds. This

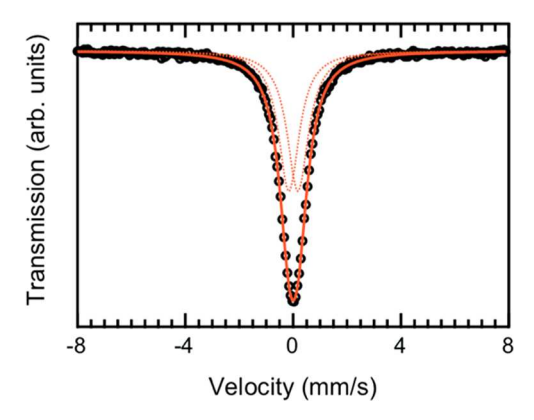


Figure 4. 119 Sn Mössbauer spectrum at room temperature for $Sr_3Sn_2O_7$. The black circles and red solid line represent the experimental data and calculated curve, respectively. The red dotted curves depict a doublet component arising due to quadrupole splitting.

result completely excludes the presence of $\mathrm{Sn^{2+}}$ in our sample. The Mössbauer spectrum is well-reproduced by an unresolved quadrupole doublet with an isomer shift of 0.01 mm/s and a quadrupole splitting of 0.33 mm/s. The small value of quadrupole splitting indicates highly symmetrical octahedral coordination for $\mathrm{Sn^{4+}}$ with a small electric field gradient, and it is consistent with the small distortion of $\mathrm{SnO_6}$ octahedra as demonstrated by the aforementioned structural analysis.

Temperature dependence of SHG intensity of Sr₃Sn₂O₇. Temperature dependence of SHG intensity of Sr₃Sn₂O₇ is displayed in Figure 5a. The SHG signal decreases

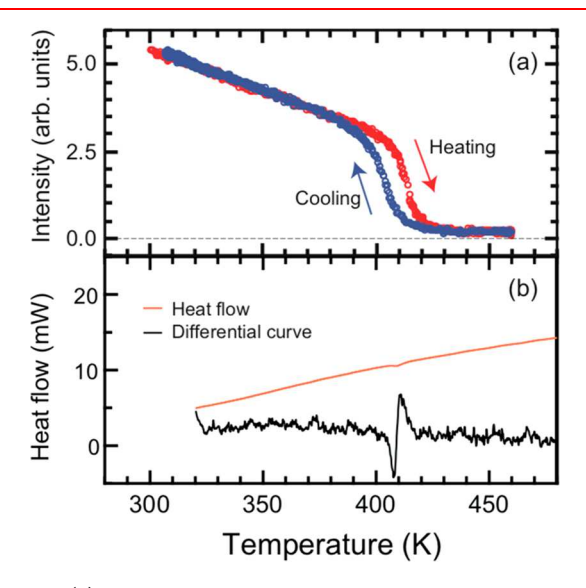


Figure 5. (a) Temperature dependence of SHG intensity of $Sr_3Sn_2O_7$ on heating (red) and cooling (blue). (b) DSC curve of $Sr_3Sn_2O_7$ on heating with the differential curve.

with increasing temperature and drops to zero at 420 K, which indicates a phase transition from the noncentrosymmetric and polar $A2_1am$ phase to a centrosymmetric and nonpolar one. Notably, SHG intensity on cooling behaves differently from that on heating; a substantial hysteresis (~10 K) was clearly observed between heating and cooling curves. The DSC curve on heating (Figure 5b) shows an endothermic peak at 410 K, where the SHG intensity presents a hysteresis. These features suggest that $Sr_3Sn_2O_7$ undergoes a first-order ferroelectric-to-

paraelectric transition at around $T_{\rm C}$ = 410 K, in contrast to the previous report, where temperature-dependent resistivity data suggested that $T_{\rm C}$ might be beyond 1035 K.³⁶

To examine the appropriate crystal symmetry of the centrosymmetric phase, we here utilize ND and SXRD patterns collected at 500 K, a temperature slightly above $T_{\rm C}$. At this temperature, the enlarged orthorhombic $\sqrt{2a_{\rm p}} \times \sqrt{2a_{\rm p}} \times c_{\rm p}$ unit cell remains unchanged, as confirmed by the superlattice reflection and the peak splitting (Figures 2a–c and 6a). A detailed inspection of the ND pattern shown in Figure

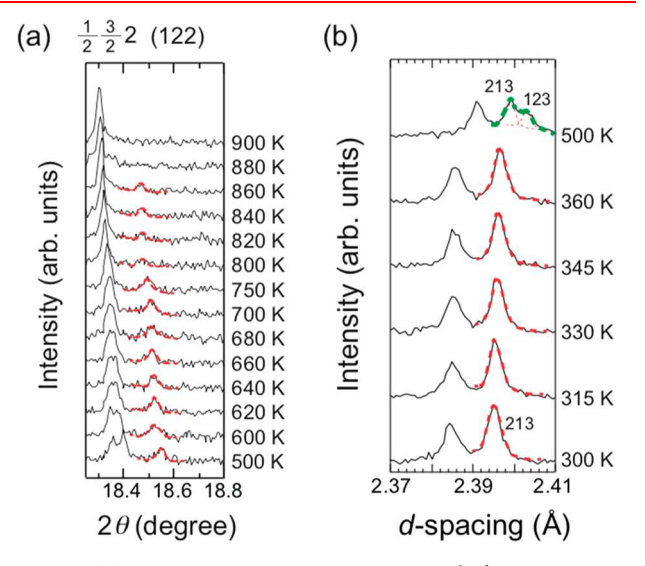


Figure 6. (a) Temperature evolution of SXRD $^{1}/_{2}^{3}/_{2}2$ superlattice reflection observed for $\mathrm{Sr_{3}Sn_{2}O_{7}}$ ($\lambda=0.800$ 484 Å). Miller indices with respect to the $\sqrt{2a_{\mathrm{p}}}\times\sqrt{2a_{\mathrm{p}}}\times c_{\mathrm{p}}$ unit cell are given in parentheses. (b) Enlarged view of the temperature-variable ND pattern for $\mathrm{Sr_{3}Sn_{2}O_{7}}$, highlighting an additional 123 reflection, which is indexed by the $\sqrt{2a_{\mathrm{p}}}\times\sqrt{2a_{\mathrm{p}}}\times c_{\mathrm{p}}$ unit cell.

6b reveals some additional Bragg reflections upon heating to 500 K. As an example, the 123 reflection appears in the *d*-range of 2.39-2.41 Å, which is forbidden under the integral reflection condition of A-face centered lattices (hkl: k + l =2n). The appearance of additional reflections signifies that the Bravais lattice type changes from oA (orthorhombic A-centered lattice) to oP (orthorhombic primitive lattice). Taking into account the lattice type, oP, extinction rules derived from Figure 2a (0kl: k + l = 2n or nothing) and assuming the compatibility with n = 2 RP structures, ⁷⁷ the plausible space groups are Pnam, Pnab, and Pnnm. Under these symmetries, rotational/tilting distortions represented by $a^-a^-c^+/a^-a^--(c^+)$, $a^-a^-c^-$, and $a^-b^-c^0$ are allowed, respectively. The $a^-a^-c^+$ $a^{-}a^{-}(c^{+})$ -type distortion describes the cooperative structural distortion, where the OORs in each perovskite layer are inphase but the direction of the rotation inverts between adjacent layers.⁷⁸ Owing to the high sensitivity of ND to oxygen positions and thus rotational/tilting distortion patterns, we can determine a possible space group through Rietveld analysis. A structural model refined in Pnab symmetry provides a best fit to the ND pattern (Figure 7a) with a small agreement factor ($R_{\text{wp}} = 13.3\%$). The agreement factors for the *Pnam* and Pnnn models are worse ($R_{wp} = 15.7\%$ and 16.6%, respectively), and the fitting curves for these two models more poorly capture the observed intensity, as shown in Figure 7b. The Rietveld refinement with the Pnab model against the 500 K SXRD pattern also converges successfully (Figure S2, SI).

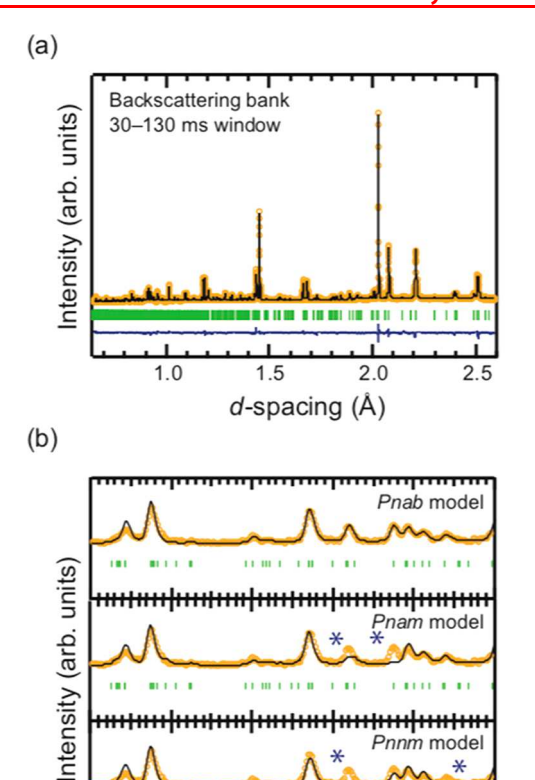


Figure 7. (a) Rietveld plot of ND data at 500 K for Sr₃Sn₂O₇ refined with a Pnab structural model. (b) An enlarged view of Rietveld plots of 500 K ND data for Sr₃Sn₂O₇ refined with Pnab, Pnam, and Pnnm structural models. Mismatches between the observed and calculated intensities are marked with asterisks. Orange circles and black and blue lines represent the observed, calculated, and difference profiles, respectively. The green ticks show the position of Bragg reflections.

1.34

1.36

d-spacing (Å)

1.30

1.32

Pnnm mode

1.38

These analyses clearly support the assignment of the orthorhombic Pnab structure to the paraelectric phase over the Pnam and Pnnm structures. The structural parameters of the Pnab phase at 500 K obtained from joint refinements against the ND and SXRD data are summarized in Table 2.

The distortion pattern in the paraelectric Pnab phase, $a^-a^-c^-$, is a combination of $a^-a^-c^0$ -type OOT (irrep X_3^-) and $a^0a^0c^-$ -type OOR (irrep X_1^-). Although out-of-phase OOT occurs in both the ferroelectric A21am and paraelectric Pnab phases, there is a marked change in the sense of OOR across the ferroelectric-to-paraelectric transition; an in-phase OOR in the $A2_1am$ phase, corresponding to an X_2^+ mode $(a^0a^0c^+)$, disappears, and out-of-phase X_1^- mode $(a^0a^0c^-)$ condenses in Pnab phase. There are no pathways along which the $a^0a^0c^+$ type OOR transforms directly and continuously to the $a^0a^0c^{-}$ type OOR. Therefore, such a structural transformation should occur discontinuously, that is, the ferroelectric-to-paraelectric transition will be of first-order. The first-order character of the ferroelectric transition is experimentally confirmed by temperature-variable SXRD data, as described in section 4, which show that the A21am and Pnab phases coexist with a substantial hysteresis on heating and cooling across the phase transition ($T_{\rm C} \sim 410$ K). The temperature evolution of the lattice parameters (a, b, and c) displays an obvious discontinuity around $T_{\rm C}$ (Figure S6, SI), validating the firstorder nature of the ferroelectric transition.

Next, we identify the structural phase transitions at temperatures higher than $T_{\rm C}$ (~410 K). The 033 reflection gets weaker and completely disappears at 750 K (Figure 2a), although other reflections (e.g., the 322 reflection), indicative of the cell doubling, are still visible (Figure 2b). The 033 reflection represents an example of 0kl (k + l = 2n) reflections that result from a condensation of the X_3^- mode, and hence, the disappearance of the 033 reflection indicates the loss of $a^-a^-c^0$ type OOT in the *Pnab* phase. An n = 2 RP structure involving only $a^0a^0c^-$ -type OOR adopts the space group Acaa. Indeed, the structural model in orthorhombic Acaa symmetry captures the ND pattern at 750 K well (Figure S3, SI). Since the orthorhombic splitting apparently disappears at 750 K (Figure 2c), we also carried out comparative refinements using tetragonal hettotype structures $(P4_2/mnm \text{ and } P4_2/mcm)$; however, these tetragonal models are ruled out by their poor fits to the collected ND pattern (Figure S4, SI). Thus, the lattice behavior shown in Figure 2c is attributed to the pseudotetragonal symmetry of the orthorhombic Acaa phase.

Finally, we identify the phase transition from the Acaa to I4/mmm structure through the temperature-variable ND and SXRD data. For ND data, all the superlattice reflections (e.g., the 322 reflection in Figure 2b) disappear at 950 K, where the sample adopts the tetragonal I4/mmm aristotype structure. The SXRD data with a fine-temperature interval allow us to determine the phase-transition temperature. As shown in Figure 6a, the SXRD superlattice 122 reflection disappears at 880 K, indicating the structural phase transition to the aristotype phase.

Table 2. Structural Parameters of Sr₃Sn₂O₇ at 500 K Obtained from Joint Refinements with a Pnab Model against ND and SXRD Data^a

atom	site	\boldsymbol{x}	y	z	$U_{\rm iso}$ or $U_{\rm eq}$ (Å ²)
O1 ^b	4 <i>a</i>	0.75	0.7116(15)	0	0.021(4)
O2	8 <i>b</i>	0.9813(14)	0.0205(12)	0.91081(14)	0.0119(13)
$O3^b$	8 <i>b</i>	0.753(3)	0.7780(11)	0.80352(13)	0.017(3)
O4	8 <i>b</i>	0.0293(14)	0.0274(13)	0.60290(17)	0.0155(14)
Sr1 ^b	4 <i>a</i>	0.75	0.2500(12)	0	0.0147(17)
Sr2 ^b	8 <i>b</i>	0.7553(12)	0.2427(7)	0.81159(7)	0.0137(12)
Sn	8 <i>b</i>	0.7503(11)	0.7493(7)	0.9016(7)	0.0035(2)

^aSpace group *Pnab* (No. 60), Z = 4. The occupancy parameter is fixed to unity for all atoms. ^bRefined anisotropically. Cell parameters: a = 5.71718(10) Å, b = 5.73526(10) Å, and c = 20.74162(7) Å. ND: $R_{wp} = 13.3\%$, $R_{B} = 7.59\%$, and $\chi^{2} = 5.44$. SXRD: $R_{wp} = 13.7\%$, $R_{B} = 3.88\%$, and $\chi^{2} = 13.7\%$, $R_{B} = 13.7\%$, $R_{C} = 13.7\%$ = 6.87.

Our diffraction studies coupled with optical SHG measurements thus unveil the sequence of structural phase transitions of n = 2 RP $Sr_3Sn_2O_7$; the ferroelectric-to-paraelectric transition of Sr₃Sn₂O₇ is observed for the first time. The phase transitions connecting the ferroelectric A2₁am phase to the nondistorted paraelectric I4/mmm phase proceed through the following sequence: $A2_1am\ (a^-a^-c^+) \rightarrow Pnab\ (a^-a^-c^-) \rightarrow$ Acaa $(a^0a^0c^-) \rightarrow I4/mmm (a^0a^0c^0)$. The ferroelectric $(A2_1am)$ to-paraelectric (Pnab) transition involves an unusual change in the sense of OOR while the OOT remains unchanged. On heating above T_C , the $a^-a^-c^0$ -type OOT disappears in the *Pnab* \rightarrow Acaa transition, and then the $a^0a^0c^-$ -type OOR finally vanishes, resulting in the I4/mmm aristotype. The lattice parameters evolve continuously across the two structural phase transitions above $T_{\rm C}$ (Figure S6, SI). Indeed, the two pairs of space groups, Pnab-Acaa and Acaa-I4/mmm, are in groupsubgroup relationships, and the $Pnab \rightarrow Acaa$ and $Acaa \rightarrow I4/$ mmm transitions are allowed to be second-order, i.e., continuous. The phase diagram and crystal structures of the observed four phases are summarized in Figure 1.

4. DISCUSSION

Verification of the Hybrid Improper Ferroelectricity in Sr₃Sn₂O₇. Hybrid improper ferroelectrics are phenomenologically characterized by the presence of the specific term, PQ_1Q_2 , in their free-energy series, where P is the macroscopic polarization and Q_1 and Q_2 are the mode amplitudes of two distinct nonpolar distortions. 11 Given the form of the trilinear term $PQ_{X_2}Q_{X_2}$ of n = 2 RP hybrid improper ferroelectrics, the polarization would be proportional to a hybrid order parameter, $\eta = Q_{X_3} Q_{X_2}$, where Q_{X_3} and Q_{X_2} are the amplitude of X_2^- and X_2^+ modes, respectively. To verify experimentally this behavior in the polar A21am phase of Sr3Sn2O7, we compare the temperature dependence of the SHG intensity (I_{SHG}) and η in the temperature range from 300 to 360 K. From the relationship between nonlinear optical tensor coefficients and P, the temperature dependence of the polarization can be estimated by using that of the SHG intensity: $P \propto \sqrt{I_{\rm SHG}}$. ^{69,75} The η values are obtained through a symmetry-mode analysis of the refined structures with the aid of AMPLIMODES software.⁷¹ Figure 8 illustrates that the temperature dependence of η has a similar trend to that of $\sqrt{I_{\rm SHG}}$, and thus, the macroscopic polarization is proportional to η . This result strongly supports the existence of an anharmonic coupling

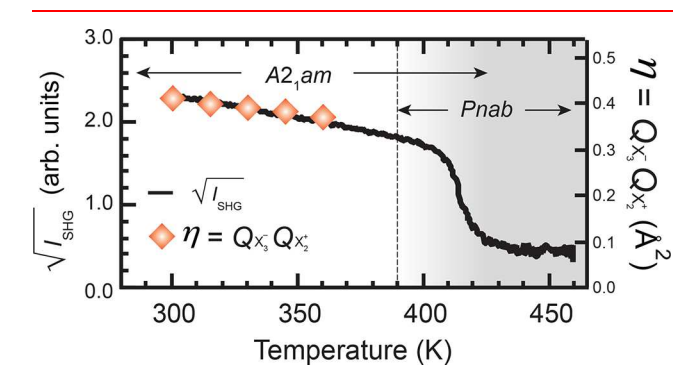


Figure 8. Temperature dependence of the square root of SHG intensity, $\sqrt{I_{\rm SHG}}$, and the hybrid order parameter, $\eta = Q_{\rm X_3^-}Q_{\rm X_2^+}$, for ${\rm Sr_3Sn_2O_7}$.

between the OOR and OOT modes and the polar displacement. Our DFT calculations (see section S4, SI) also revealed that the OOR and OOT serve as the primary order parameters inducing the $A2_1am$ polar structure and that the polar displacement is just a byproduct of the rotational/tilting distortions. Our experimental and first-principles results prove the chemical intuition that $Sr_3Sn_2O_7$ is an ideal hybrid improper ferroelectric, for which a proper mechanism driven by the SOJT effect plays no role at all in stabilizing the ferroelectric phase.

Universal Relationship of Curie Temperatures and **Tolerance Factors.** So far, we have demonstrated that n = 2RP $Sr_3Sn_2O_7$ is a hybrid improper ferroelectric with $T_C = 410$ K, where the polar distortion is induced by a combination of OOR $(Q_{X_{-}})$ and OOT $(Q_{X_{-}})$ interacting through a trilinear term of the form $PQ_{X_3}^-Q_{X_2}^+$. Since the OOR and OOT distortions arise from the size mismatch of A- and B-site cations, it is interesting to examine the effect of changing the A-site cation size on rotational/tilting distortions and, hence, on the ferroelectric transition. We additionally prepared a Casubstituted series, $(Sr_{1-x}Ca_x)_3Sn_2O_7$ (x = 0.1 and 0.2), and investigated their thermally induced phase-transition behavior, including ferroelectric-to-paraelectric transitions. The characterization by ND, SXRD, and 119Sn Mössbauer spectroscopy revealed that the Ca-substituted series (x = 0.1 and 0.2) also adopt the ferroelectric A2₁am structure at 300 K (Figures S12 and S14, SI), with the Sn ions being present in a tetravalent state (Figure S11, SI). The lattice parameters (a, b, and c) at 300 K obtained from joint refinements against the ND and SXRD data decrease with the substitution of a smaller cation (i.e., Ca²⁺) for Sr²⁺ on the A-site (see Table 1, and Tables S3 and S5, SI).

In order to probe the ferroelectric transition behavior, we utilize temperature-dependent SXRD patterns. Figure 9a-c displays the evolution of SXRD 0010 reflections of $(Sr_{1-x}Ca_x)_3Sn_2O_7$ (x = 0, 0.1, and 0.2) upon heating and cooling cycle. We see two-phase coexistence and hysteresis around 410 K for x = 0 (Figure 9a), 590 K for x = 0.1 (Figure 9b), and 800 K for x = 0.2 (Figure 9c), indicative of a firstorder phase transition. Similar to the case of $Sr_3Sn_2O_7$ (x = 0), the SXRD patterns of Ca-substituted series at temperatures slightly above the phase transitions (i.e., 650 and 860 K for x =0.1 and 0.2, respectively) are well fitted based on the structural model in Pnab symmetry (Figures S13 and S15, SI). Thus, we identify a first-order ferroelectric (A21am)-toparaelectric (Pnab) transition for $(Sr_{1-x}Ca_x)_3Sn_2O_7$ solid solutions as well. The weight fraction of the ferroelectric $A2_1am$ phase in the two-phase coexistence $(A2_1am + Pnab)$ regions for x = 0, 0.1, and 0.2 samples is plotted in Figure 9d as a function of temperature. We define $T_{\rm C}$ as the center of the thermal hysteresis curve. We see that for x = 0 the hysteresis loop of the ferroelectric phase fraction in the vicinity of T_C follows completely that of the SHG intensity, as depicted in Figure 5a (see also Figure S16, SI). As expected from the geometric origin of the hybrid improper ferroelectricity, the introduction of a smaller A-site cation, i.e., the partial substitution of Ca^{2+} for Sr^{2+} (x = 0.1 and 0.2), enhances the magnitudes of OOR and OOT, resulting in higher $T_{\rm C}$ values.

To quantitatively describe the rotational/tilting distortion preference, we introduce the Goldschmidt tolerance factor, t, which gives a simple measure of the size mismatch of constituent cations. Shannon's six-coordinate ionic radii⁷⁹ are

Journal of the American Chemical Society

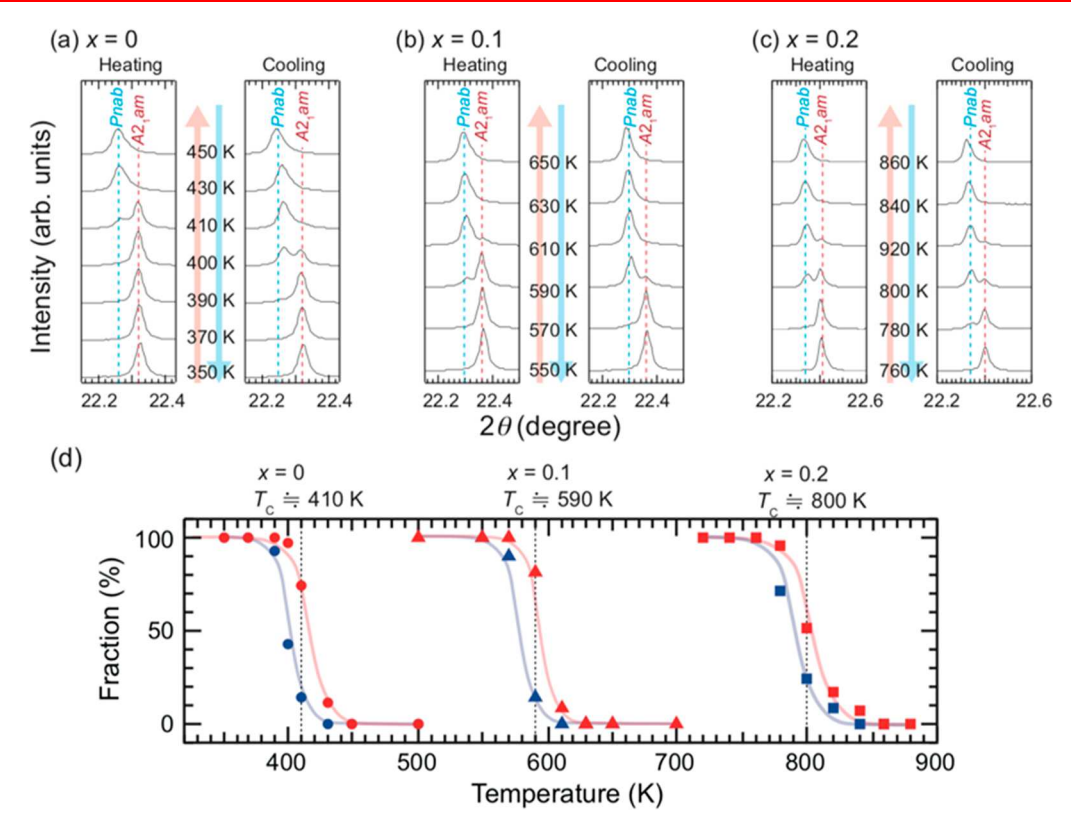


Figure 9. (a–c) Temperature dependence of the SXRD (λ = 0.800 484 Å) 0010 reflection of $(Sr_{1-x}Ca_x)_3Sn_2O_7$ (x = 0, 0.1, and 0.2) on heating and cooling across the ferroelectric-to-paraelectric transition between $A2_1am$ and Pnab phases. (d) Temperature evolution of the weight fraction of ferroelectric $A2_1am$ phase of $(Sr_{1-x}Ca_x)_3Sn_2O_7$ (x = 0, 0.1, and 0.2) on heating (red) and cooling (blue). Circles, triangles, and squares represent the calculated values from multiphase Rietveld refinements against SXRD data for x = 0, 0.1, and 0.2 samples, respectively, and the solid lines are given to guide the eye. The vertical dashed line for each sample indicates the center of hysteresis, corresponding to the ferroelectric-to-paraelectric transition temperature (T_C); $T_C \sim 410$ K for x = 0, $T_C \sim 590$ K for x = 0.1, and $T_C \sim 800$ K for x = 0.2.

used here. A nondistorted structure forms with $t \sim 1.0$, whereas for smaller t values (0.8 < t < 1.0), the A-site cation is too small for its site, resulting in a low-symmetry structure with rotated and/or tilted BO₆ octahedra. Figure 10 plots the $T_{\rm C}$ values of the (Sr_{1-x}Ca_x)₃Sn₂O₇ (x = 0, 0.1, and 0.2) system as a

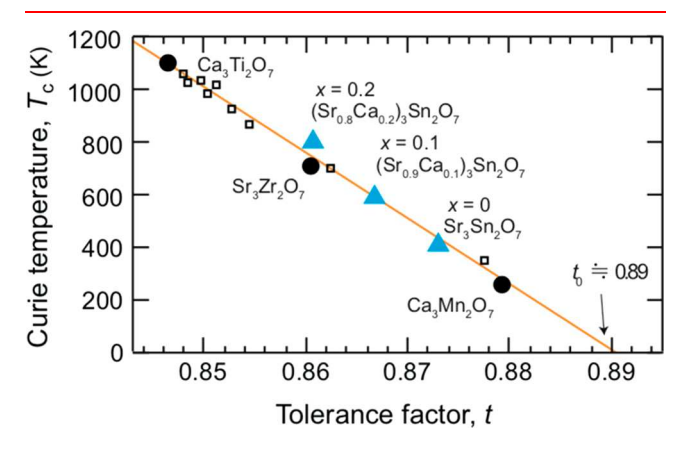


Figure 10. Curie temperatures $(T_{\rm C})$ of n=2 RP ferroelectrics against the tolerance factor (t) of their perovskite unit. The result of linear fitting is depicted by an orange line with the critical t value, t_0 . Blue triangles represent the data for $({\rm Sr_{1-x}Ca_x})_3{\rm Sn_2O_7}$ (x=0,0.1, and 0.2) obtained in this work. The black circles show the data previously reported for ${\rm Ca_3Ti_2O_7}^{32}$ ${\rm Sr_3Zr_2O_7}^{37}$ and ${\rm Ca_3Mn_2O_7}^{40}$ The squares indicate the reported data for solid-solution systems $({\rm Ca_3Sr})_3{\rm Ti_2O_7}^{34}$ and ${\rm Ca_3(Ti_3Mn})_2{\rm O_7}^{3.2,35}$

function of t. T_C is found to monotonically increase with decreasing t. Because of the ubiquity of t in characterizing perovskite units, we can extend the compositional range to other n = 2 RP ferroelectrics. In addition to $(Sr,Ca)_3Sn_2O_7$, we consider 12 known RP compounds, i.e., $Ca_3Ti_2O_7$, $^{32}Ca_3Mn_2O_7$, $^{40}Sr_3Zr_2O_7$, $^{37}(Ca_3Sr)_3Ti_2O_7$, 34 and $Ca_3(Ti_7Mn)_2O_7$. In the suite of 15 different $A_3B_2O_7$ ferroelectrics, $T_{\rm C}$ values range from below room temperature (~280 K) to about 1100 K. We find a linear relationship between $T_{\rm C}$ and t (Figure 10). Given the chemical diversity of n=2 RP phases, the strong correlation between $T_{\rm C}$ and t is remarkable. From a linear extrapolation of this relation, one can see that an n = 2 RP phase with t = 0.89 has $T_C = 0$ K. In other words, t = 0.89 is an upper limit, t_0 , for an n = 2 RP phase to crystallize in a ferroelectric A21am structure. Recent theoretical calculations also revealed that the ferroelectric $A2_1am$ structure is destabilized when t > 0.89; $Ca_3Ge_2O_7$ (t =0.879) has the $A2_1am$ ground state, whereas $Sr_3Tc_2O_7$ (t = 0.892) exhibits a tilted but nonpolar P42/mnm ground structure.⁵¹ Although local structural disorder exists in solid solutions of $A_3B_2O_7$ ferroelectric, it has little effect on T_C , and hence, the average t values strongly correlate with $T_{\rm C}$. The minor effect of local structural disorder on $T_{\rm C}$ was also observed for ferroelectric Pb(Zr_{1-x}Ti_x)O₃ solid solutions, where $T_{\rm C}$ is a smooth and monotonic function of x.⁸⁰ The universal relationship shown in Figure 10 proves a controllability of $T_{\rm C}$ over a wide temperature range with the geometric effect (ionic size mismatch) in hybrid improper ferroelectrics. The close relationship between T_C and t provides a useful guide for designing materials with the desired properties for a given application and also for predicting $T_{\rm C}$ of as yet unsynthesized materials.

Previously, Abrahams et al.⁸¹ have reported a simple relationship between Curie temperature and polarization, T_C $\propto P^2$, for proper ferroelectrics such as BaTiO₃. According to this report, we also explore the relationships between P and T_C in hybrid improper ferroelectrics. A recent theoretical study on hybrid improper ferroelectric $A_3B_2O_7$ compounds (A = Mg, Ca, and Sr; B = Zr, Sn, and Ge) revealed that the P values calculated by using the Born effective charge are a smooth and monotonic function of t (Figure S17, SI). One can find a linear relationship between P and t. From this result (Figure S17, SI) and the linear relationship between T_C and t (Figure 10), we expect $T_{\rm C} \propto P$ for hybrid improper ferroelectrics, in contrast to the case of proper ferroelectrics. For Ca₃Ti₂O₇, ³² $Ca_3Mn_2O_{7}$, $^{33}Sr_3Zr_2O_{7}$, 37 and $Sr_3Sn_2O_7$ ceramics, we observe that the T_C tends to correlate linearly with the experimental Pvalues obtained through ferroelectric hysteresis measurements (Figure S18, SI). It should be noted that the P values were measured for polycrystalline samples. The polarization measurements for single crystals will provide more reliable verification of the relationship between T_C and P.

Interestingly, all the A₃B₂O₇ compounds listed in Figure 10 exhibit the first-order nature of the ferroelectric transition. For Ca₃Ti₂O₇ and Ca₃(Ti,Mn)₂O₇, the first-order transition between the ferroelectric $A2_1am$ $(a^-a^-c^+)$ and nondistorted I4/mmm ($a^0a^0c^0$) phases has been suggested on the basis of the DSC and SXRD results.³² As for the other compounds, the first-order ferroelectric transition is characterized by a competition between the ferroelectric A21am phase and a distorted nonpolar polymorph. In the case of Sr₃Zr₂O₇, the competing metastable polymorph to the A21am phase has Pnab symmetry involving an $a^-a^-c^-$ -type distortion.³⁷ The *Pnab* phase originates from a trilinear coupling of the OOR and OOT modes interacting with an antipolar mode, i.e., hybrid improper "antiferroelectric" mechanism; the antipolar mode leads to a complete cancellation of the layer polarization, providing no net macroscopic polarization (Figure 1a). Namely, there is a competition between hybrid improper ferroelectric and antiferroelectric mechanisms in Sr₃Zr₂O₇. This result corroborates the theoretical prediction 50,51 and shows the importance of understanding anharmonic interactions among lattice degrees of freedom. The title compounds, (Sr,Ca)₃Sn₂O₇, undergo the same ferroelectric transition (A2₁am-to-Pnab) as Sr₃Zr₂O₇, as a result of a competition between hybrid improper ferroelectric and antiferroelectric mechanisms (see section S4, SI), again highlighting the interplay between the anharmonic interactions active in layered oxides. For (Ca,Sr)₃Mn₂O₇ system^{39,40} with relatively larger t values, a nonpolar polymorph with Acaa symmetry involving only $a^0a^0c^-$ -type OOR is observed as the competing metastable phase to the A21am phase. The Acaa phase exhibits a uniaxial negative thermal expansion along the c axis. 82 As shown in Figure S6 (SI), we also observe a similar phenomenon, i.e., uniaxial negative thermal expansion along the c axis, in the intermediate Acaa phase for Sr₃Sn₂O₇. The two intermediate Pnab and Acaa phases, as well as the groundstate ferroelectric A2₁am phase, have novel physical properties that stem from their rotational/tilting distortions. Hence, it would be interesting to stabilize the two intermediate phases at room temperature by chemical tuning according to the T_C vs trelationship established in this work.

5. SUMMARY

In conclusion, we demonstrate that $n = 2 \text{ RP } \text{Sr}_3 \text{Sn}_2 \text{O}_7$ is an ideal hybrid improper ferroelectric, where the SOJT effect plays no role at all in driving the ferroelectric transition. Instead, the nonpolar OOR and OOT distortions trilinearly couple to create the ferroelectric polarization as a byproduct. In contrast to the previous report, 36 we observe a first-order ferroelectric-to-paraelectric transition in $Sr_3Sn_2O_7$ ($T_C = 410$ K). We also show that the isovalent substitution of Ca²⁺ for Sr^{2+} , which leads to a decrease in t, increases T_C up to 800 K. Remarkably, we find a linear relationship between T_C and tacross the suite of 15 A₃B₂O₇ compounds consisting of RP ferroelectrics reported here and those reported previously elsewhere. This relationship provides a predictive guideline for estimating the T_C of a given perovskite-derived compound, which would complement the design approach blending group theory and first principles. Further, the findings open routes to the possible use of hybrid improper ferroelectrics in technological applications, for example, pyroelectric energy harvesting, $^{83-85}$ where the tunability of $T_{\rm C}$ is advantageous for achieving a large electrothermal coupling factor.

ASSOCIATED CONTENT

S Supporting Information

The Supporting Information is available free of charge on the ACS Publications website at DOI: 10.1021/jacs.8b07998.

Additional ND and SXRD analyses, first-principles calculation results, and Mössbauer spectroscopy (PDF)

AUTHOR INFORMATION

Corresponding Author

*fujita.koji.5w@kyoto-u.ac.jp

ORCID ©

Arnab Sen Gupta: 0000-0002-0801-6555 Shunsuke Murai: 0000-0002-4597-973X James M. Rondinelli: 0000-0003-0508-2175 Venkatraman Gopalan: 0000-0001-6866-3677

Koji Fujita: 0000-0002-1700-0889

Present Address

OH.A.: Department of Applied Chemistry, Kyushu University, Motooka, Fukuoka 819-0395, Japan

The authors declare no competing financial interest.

ACKNOWLEDGMENTS

This work was supported by the JSPS KAKENHI (Grant Numbers JP16H04496, JP17H01320, JP18K8940, JP17K19172, JP18H01892), the Grant-in-Aid for JSPS Research Fellow (Grant Number JP17J07106), and the National Science Foundation Penn State Center for Nanoscale Science MRSEC grant number DMR-1420620 and DMR-1807768. SXRD experiments were performed on BL02B2 at SPring-8 with the approval of JASRI (Proposal Nos. 2017B11423 and 2018A1391). Time-of-flight ND experiments on HRPD at the ISIS Pulsed Neutron and Muon Source were supported by beam time allocations from STFC (RB1620102 and XB1790074). The Mössbauer spectroscopic measurements were performed under the Nanotechnology Platform Program by MEXT, Japan.

REFERENCES

- (1) Scott, J. F. Science 2007, 315, 954-959.
- (2) Cohen, R. E. Nature 1992, 358, 136-138.
- (3) Hill, N. A. J. Phys. Chem. B 2000, 104, 6694-6709.
- (4) Bersuker, I. B. Phys. Rev. Lett. 2012, 108, 137202.
- (5) Rondinelli, J. M.; Eidelson, A. S.; Spaldin, N. A. Phys. Rev. B: Condens. Matter Mater. Phys. 2009, 79, 205119.
- (6) Walsh, A.; Payne, D. J.; Egdell, R. G.; Watson, G. W. Chem. Soc. Rev. 2011, 40, 4455-4463.
- (7) Koopmans, H. J. A.; Van De Velde, G. M. H.; Gellings, P. J. Acta Crystallogr., Sect. C: Cryst. Struct. Commun. 1983, 39, 1323-1325.
- (8) Ahtee, A.; Ahtee, M.; Glazer, A. M.; Hewat, A. W. Acta Crystallogr., Sect. B: Struct. Crystallogr. Cryst. Chem. 1976, 32, 3243-
- (9) Levin, I.; Amos, T. G.; Bell, S. M.; Farber, L.; Vanderah, T. A.; Roth, R. S.; Toby, B. H. J. Solid State Chem. 2003, 175, 170-181.
- (10) Sawaguchi, E. J. Phys. Soc. Jpn. 1953, 8, 615-629.
- (11) Benedek, N. A.; Fennie, C. J. Phys. Rev. Lett. 2011, 106, 107204.
- (12) Benedek, N. A.; Mulder, A. T.; Fennie, C. J. J. Solid State Chem. 2012, 195, 11-20.
- (13) Harris, A. B. Phys. Rev. B: Condens. Matter Mater. Phys. 2011, 84, 064116.
- (14) Bousquet, E.; Dawber, M.; Stucki, N.; Lichtensteiger, C.; Hermet, P.; Gariglio, S.; Triscone, J.-M.; Ghosez, P. Nature 2008, 452,
- (15) Mulder, A. T.; Benedek, N. A.; Rondinelli, J. M.; Fennie, C. J. Adv. Funct. Mater. 2013, 23, 4810.
- (16) Ruddlesden, S. N.; Popper, P. Acta Crystallogr. 1957, 10, 538-539.
- (17) Benedek, N. A. Inorg. Chem. 2014, 53, 3769-3777.
- (18) Benedek, N. A.; Rondinelli, J. M.; Djani, H.; Ghosez, P.; Lightfoot, P. Dalt. Trans. 2015, 44, 10543-10558.
- (19) Young, J.; Stroppa, A.; Picozzi, S.; Rondinelli, J. M. J. Phys.: Condens. Matter 2015, 27 (28), 283202.
- (20) Boström, H. L. B.; Senn, M. S.; Goodwin, A. L. Nat. Commun. 2018, 9, 2380.
- (21) Karen, V. L.; Hellenbrandt, M. Acta Crystallogr., Sect. A: Found. Crystallogr. 2002, 58, c367.
- (22) Rondinelli, J. M.; Fennie, C. J. Adv. Mater. 2012, 24, 1961-1968
- (23) Young, J.; Rondinelli, J. M. Chem. Mater. 2013, 25, 4545-4550.
- (24) An, M.; Zhang, H.-M.; Weng, Y.-K.; Zhang, Y.; Dong, S. Front. Phys. 2016, 11, 117501.
- (25) Balachandran, P. V.; Puggioni, D.; Rondinelli, J. M. Inorg. Chem. 2014, 53, 336-348.
- (26) Young, J.; Stroppa, A.; Picozzi, S.; Rondinelli, J. M. Dalt. Trans. **2015**, 44, 10644-10653.
- (27) Zhao, H. J.; Ren, W.; Yang, Y.; Íñiguez, J.; Chen, X. M.; Bellaiche, L. Nat. Commun. 2014, 5, 4021.
- (28) Balachandran, P. V.; Young, J.; Lookman, T.; Rondinelli, J. M. Nat. Commun. 2017, 8, 14282.
- (29) Puggioni, D.; Rondinelli, J. M. Nat. Commun. 2014, 5, 3432.
- (30) Sim, H.; Cheong, S. W.; Kim, B. G. Phys. Rev. B: Condens. Matter Mater. Phys. 2013, 88, 014101.
- (31) Oh, Y. S.; Luo, X.; Huang, F.-T.; Wang, Y.; Cheong, S.-W. Nat. Mater. 2015, 14, 407-413.
- (32) Liu, X. Q.; Wu, J. W.; Shi, X. X.; Zhao, H. J.; Zhou, H. Y.; Qiu, R. H.; Zhang, W. Q.; Chen, X. M. Appl. Phys. Lett. 2015, 106, 202903.
- (33) Liu, M.; Zhang, Y.; Lin, L.-F.; Lin, L.; Yang, S.; Li, X.; Wang, Y.; Li, S.; Yan, Z.; Wang, X.; Li, X.-G.; Dong, S.; Liu, J.-M. Appl. Phys. Lett. 2018, 113, 022902.
- (34) Li, G. J.; Liu, X. Q.; Lu, J. J.; Zhu, H. Y.; Chen, X. M. J. Appl. Phys. 2018, 123, 014101.
- (35) Gao, B.; Huang, F.-T.; Wang, Y.; Kim, J.-W.; Wang, L.; Lim, S.-J.; Cheong, S.-W. Appl. Phys. Lett. 2017, 110, 222906.
- (36) Wang, Y.; Huang, F.-T.; Luo, X.; Gao, B.; Cheong, S.-W. Adv. Mater. 2017, 29, 1601288.
- (37) Yoshida, S.; Fujita, K.; Akamatsu, H.; Hernandez, O.; Sen Gupta, A.; Brown, F. G.; Padmanabhan, H.; Gibbs, A. S.; Kuge, T.;

- Tsuji, R.; Murai, S.; Rondinelli, J. M.; Gopalan, V.; Tanaka, K. Adv. Funct. Mater. 2018, 28, 1801856.
- (38) Li, X.; Yang, L.; Li, C. F.; Liu, M. F.; Fan, Z.; Xie, Y. L.; Lu, C. L.; Lin, L.; Yan, Z. B.; Zhang, Z.; Dai, J. Y.; Liu, J.-M.; Cheong, S.-W. Appl. Phys. Lett. 2017, 110, 042901.
- (39) Senn, M. S.; Murray, C. A.; Luo, X.; Wang, L.; Huang, F.-T.; Cheong, S.-W.; Bombardi, A.; Ablitt, C.; Mostofi, A. A.; Bristowe, N. C. J. Am. Chem. Soc. 2016, 138, 5479-5482.
- (40) Senn, M. S.; Bombardi, A.; Murray, C. A.; Vecchini, C.; Scherillo, A.; Luo, X.; Cheong, S. W. Phys. Rev. Lett. 2015, 114,
- (41) Strayer, M. E.; Gupta, A. S.; Akamatsu, H.; Lei, S.; Benedek, N. A.; Gopalan, V.; Mallouk, T. E. Adv. Funct. Mater. 2016, 26, 1930-1937.
- (42) Dixon, C.; McNulty, J.; Knight, K.; Gibbs, A.; Lightfoot, P. Crystals 2017, 7, 135.
- (43) Pitcher, M. J.; Mandal, P.; Dyer, M. S.; Alaria, J.; Borisov, P.; Niu, H.; Claridge, J. B.; Rosseinsky, M. J. Science 2015, 347, 420-424.
- (44) Zhu, T.; Cohen, T.; Gibbs, A. S.; Zhang, W.; Halasyamani, P. S.; Hayward, M. A.; Benedek, N. A. Chem. Mater. 2017, 29, 9489-
- (45) Young, J.; Moon, E. J.; Mukherjee, D.; Stone, G.; Gopalan, V.; Alem, N.; May, S. J.; Rondinelli, J. M. J. Am. Chem. Soc. 2017, 139, 2833-2841.
- (46) Retuerto, M.; Li, M. R.; Ignatov, A.; Croft, M.; Ramanujachary, K. V.; Chi, S.; Hodges, J. P.; Dachraoui, W.; Hadermann, J.; Tran, T. T.; Halasyamani, P. S.; Grams, C. P.; Hemberger, J.; Greenblatt, M. Inorg. Chem. 2013, 52, 12482-12491.
- (47) Zhong, W.; Vanderbilt, D.; Rabe, K. M. Phys. Rev. Lett. 1994, 73, 1861-1864.
- (48) Paul, A.; Sun, J.; Perdew, J. P.; Waghmare, U. V. Phys. Rev. B: Condens. Matter Mater. Phys. 2017, 95, 054111.
- (49) Nishimatsu, T.; Iwamoto, N.; Kawazoe, Y.; Waghmare, U. V. Phys. Rev. B: Condens. Matter Mater. Phys. 2010, 82, 134106.
- (50) Lu, X.-Z.; Rondinelli, J. M. Nat. Mater. 2016, 15, 951-955.
- (51) Lu, X.-Z.; Rondinelli, J. M. Adv. Funct. Mater. 2017, 27, 1604312.
- (52) Rietveld, H. M. J. Appl. Crystallogr. 1969, 2, 65-71.
- (53) Rodríguez-Carvajal, J. Phys. B 1993, 192, 55-69.
- (54) Blöchl, P. E. Phys. Rev. B: Condens. Matter Mater. Phys. 1994, 50, 17953-17979.
- (55) Kresse, G.; Joubert, D. Phys. Rev. B: Condens. Matter Mater. Phys. 1999, 59, 1758-1775.
- (56) Perdew, J. P.; Burke, K.; Ernzerhof, M. Phys. Rev. Lett. 1996, 77, 3865-3868.
- (57) Perdew, J. P.; Burke, K.; Ernzerhof, M. Phys. Rev. Lett. 1997, 78,
- (58) Perdew, J. P.; Ruzsinszky, A.; Csonka, G. I.; Vydrov, O. A.; Scuseria, G. E.; Constantin, L. A.; Zhou, X.; Burke, K. Phys. Rev. Lett. 2008, 100, 136406.
- (59) Kresse, G.; Hafner, J. Phys. Rev. B: Condens. Matter Mater. Phys. 1993, 48, 13115-13118.
- (60) Kresse, G.; Hafner, J. Phys. Rev. B: Condens. Matter Mater. Phys. 1993, 47, 558-561.
- (61) Kresse, G.; Furthmüller, J. Comput. Mater. Sci. 1996, 6, 15-50.
- (62) Kresse, G.; Furthmüller, J. Phys. Rev. B: Condens. Matter Mater. Phys. 1996, 54, 11169-11186.
- (63) Togo, A.; Tanaka, I. Scr. Mater. 2015, 108, 1-5.
- (64) Hinuma, Y.; Togo, A.; Hayashi, H.; Tanaka, I. 2015, arXiv:cond-mat/1506.01455. arXiv.org e-Print archive. http://arxiv. org/abs/1506.01455 (accessed Nov 30, 2017).
- (65) Setyawan, W.; Curtarolo, S. Comput. Mater. Sci. 2010, 49, 299-
- (66) Hinuma, Y.; Pizzi, G.; Kumagai, Y.; Oba, F.; Tanaka, I. Comput. Mater. Sci. 2017, 128, 140-184.
- (67) Togo, A.; Tanaka, I. Phys. Rev. B: Condens. Matter Mater. Phys. 2013, 87, 184104.

- (68) Akamatsu, H.; Fujita, K.; Kuge, T.; Sen Gupta, A.; Togo, A.; Lei, S.; Xue, F.; Stone, G.; Rondinelli, J. M.; Chen, L.-Q.; Tanaka, I.; Gopalan, V.; Tanaka, K. *Phys. Rev. Lett.* **2014**, *112*, 187602.
- (69) Gupta, A. S.; Akamatsu, H.; Strayer, M. E.; Lei, S.; Kuge, T.; Fujita, K.; dela Cruz, C.; Togo, A.; Tanaka, I.; Tanaka, K.; Mallouk, T. E.; Gopalan, V. Adv. Electron. Mater. 2016, 2, 1500196.
- (70) Šen Gupta, A.; Akamatsu, H.; Brown, F. G.; Nguyen, M. A. T.; Strayer, M. E.; Lapidus, S.; Yoshida, S.; Fujita, K.; Tanaka, K.; Tanaka, I.; Mallouk, T. E.; Gopalan, V. *Chem. Mater.* **2017**, *29*, 656–665.
- (71) Orobengoa, D.; Capillas, C.; Aroyo, M. I.; Perez-Mato, J. M. J. Appl. Crystallogr. **2009**, 42, 820–833.
- (72) Momma, K.; Izumi, F. J. Appl. Crystallogr. 2011, 44, 1272–1276.
- (73) Green, M. A.; Prassides, K.; Day, P.; Neumann, D. A. Int. J. Inorg. Mater. **2000**, *2*, 35–41.
- (74) Glazer, A. M. Acta Crystallogr., Sect. B: Struct. Crystallogr. Cryst. Chem. 1972, 28, 3384–3392.
- (75) Denev, S. A.; Lummen, T. T. A.; Barnes, E.; Kumar, A.; Gopalan, V. J. Am. Ceram. Soc. 2011, 94, 2699–2727.
- (76) Greenwood, N. N.; Gibb, T. C. Mössbauer Spectroscopy; Chapman and Hall: London, 1971.
- (77) Kelsey, S. Hist. Workshop J. 1995, 40, 251–272.
- (78) Zhang, Z.; Senn, M. S.; Hayward, M. A. Chem. Mater. 2016, 28, 8399–8406.
- (79) Shannon, R. D. Acta Crystallogr., Sect. A: Cryst. Phys., Diffr., Theor. Gen. Crystallogr. 1976, 32, 751–767.
- (80) Noheda, B.; Cox, D. E.; Shirane, G.; Gonzalo, J. A.; Cross, L. E.; Park, S.-E. Appl. Phys. Lett. 1999, 74, 2059–2061.
- (81) Abrahams, S. C.; Kurtz, S. K.; Jamieson, P. B. *Phys. Rev.* **1968**, 172, 551–553.
- (82) Ablitt, C.; Craddock, S.; Senn, M. S.; Mostofi, A. A.; Bristowe, N. C. npj Comput. Mater. 2017, 3, 44.
- (83) Olsen, R. B.; Bruno, D. A.; Briscoe, J. M. J. Appl. Phys. 1985, 58, 4709–4716.
- (84) Maeda, Y.; Wakamatsu, T.; Konishi, A.; Moriwake, H.; Moriyoshi, C.; Kuroiwa, Y.; Tanabe, K.; Terasaki, I.; Taniguchi, H. *Phys. Rev. Appl.* **2017**, *7*, 034012.
- (85) Wakamatsu, T.; Tanabe, K.; Terasaki, I.; Taniguchi, H. Phys. Status Solidi RRL 2017, 11, 1700009.